الجمهورية الجزائرية الديمقراطية الشعبية
People's Democratic Republic of Algeria
وزارة التعليم العالي و البحث العلمي
Ministry of Higher Education and Scientific Research

المدرسة الوطنية العليا للتكنولوجيا و الهندسة - عنابة
National Higher School of Technology and Engineering – Annaba

Department of Process Engineering and Energetics

In Partial Fulfillment of the Requirements

for the
MASTER DEGREE

Field of Study: Chemical engineering

Presented by

Abderrahmane SELMANI

Modeling a zero-gap asymmetric electrolyzer: a fundamental approach to overcome the geometric limits

Supervised by

Dr.Kaouther Kerboua, MCA
NHSTE Annaba

Examination Board :

- Dr. Kahlerras Mohamed Said — President – NHSTE
- Dr. Nedjah Nawel — Examiner – NHSTE

Academic Year 2025

Acknowledgments

First and foremost, I would like to express my sincere gratitude to Dr. Kaouther Kerboua, who guided this work with great dedication, patience, and scientific rigor. Her valuable insights and unwavering support throughout the project shaped both the experimental and the modeling aspects of this study. I am also grateful to the technical staff and engineers of the UTE Desaladora plant in Skikda, whose collaboration and openness made the industrial training possible. Their willingness to share operational knowledge and data significantly contributed to the realism and relevance of this work. Finally, I would like to extend my heartfelt appreciation to my family and close friends for their continuous encouragement and moral support during every stage of this academic journey.

Abstract

The widespread use of reverse osmosis (RO) for seawater desalination has intensified the issue of brine disposal, raising environmental concerns due to its high salinity and chemical load. This study investigates a sustainable valorization route by coupling industrial field data from the UTE Desaladora plant in Skikda, Algeria, with a numerical model of asymmetric zero-gap electrolysis for the recovery of valuable products, notably hydrogen (H_2) and hydroxide ions (OH^-). A MATLAB-based simulation tool was developed to assess the performance of the electrolyzer under various operational parameters, including voltage, temperature, gas bubble accumulation, Faradaic efficiency, and hydroxide capture factor effects. Polarization curve, has demonstrated that anode activation significantly enhanced the system's efficiency, reducing internal resistance of nearly 70% and increasing performance by up to 65%. The performance assessment showed strong agreement between simulation and experimental results in hydrogen production while greater deviations were observed in current evolution over tome, mainly due to gas bubble accumulation and simplified assumptions in the model. The parametric study revealed that temperature increase reduced cathodic resistance by 46% and increased H_2 output by more than 60%. Similarly, bubble coverage beyond 30% drastically increased ohmic losses, while a hydroxide capture factor above 0.9 severely hindered conductivity and gas production. Discrepancies between simulation and experimental data highlighted the impact of real-world phenomena such as bubble coverage and side reactions, emphasizing the need for more comprehensive and dynamic modeling.

Key words: Reverse osmosis (RO), brine valorization, asymmetric zero gap cell, MATLAB simulation.

ملخص

الاستخدام الواسع للتناضح العكسي (RO) في تحلية مياه البحر زاد من حدة مشكلة تصريف المياه المالحة، مما يثير مخاوف بيئية بسبب ملوحتها العالية وحمولتها الكيميائية. تبحث هذه الدراسة في مسار مستدام للاستفادة من هذه المياه المالحة من خلال الجمع بين بيانات ميدانية صناعية من محطة التحلية في سكيكدة، الجزائر، ونموذج رقمي لعملية التحليل الكهربائي غير المتناظر ذات الفجوة الصفرية لاسترجاع منتجات قيمة، خاصة الهيدروجين (H_2) وأيونات الهيدروكسيد(OH^-) . تم تطوير أداة محاكاة باستخدام برنامج MATLAB لتقييم أداء المحلل الكهربائي تحت ظروف تشغيلية مختلفة، بما في ذلك الجهد الكهربائي، درجة الحرارة، تراكم فقاعات الغاز، الكفاءة الفارادية، وتأثير معامل التقاط الهيدروكسيد. أظهرت منحنيات الاستقطاب أن تنشيط المصعد أدى إلى تحسين كبير في كفاءة النظام، حيث خفض المقاومة الداخلية بنسبة تقارب 70% وزاد من الأداء بنسبة تصل إلى 65%. أظهر تقييم الأداء توافقًا قويًا بين نتائج المحاكاة والنتائج التجريبية في إنتاج الهيدروجين، بينما ظهرت انحرافات أكبر في تطور التيار مع الزمن، ويرجع ذلك أساسًا إلى تراكم فقاعات الغاز وافتراضات أكثر تبسيطا في النموذج. أظهرت الدراسة المعيارية أن زيادة درجة الحرارة خفضت المقاومة الكاثودية بنسبة 46% وزادت من إنتاج الهيدروجين بأكثر من 60%. وبالمثل، فإن تغطية الفقاعات بنسبة تتجاوز 30% أدت إلى زيادة كبيرة في الخسائر الأومية، في حين أن معامل التقاط الهيدروكسيد الأعلى من 0.9 أعاق بشدة الناقلية الايونية وإنتاج الغاز. سلطت الفروقات بين بيانات المحاكاة والبيانات التجريبية الضوء على تأثير الظواهر الواقعية مثل تغطية الفقاعات والتفاعلات الجانبية، مما يؤكد الحاجة إلى نماذج أكثر شمولاً وديناميكية.

الكلمات المفتاحية: التناضح العكسي، تثمين المحلول الملحي، خلية ذات فجوة صفرية، محاكات ماتلاب.

Résumé

L'utilisation généralisée de l'osmose inverse (RO) pour le dessalement de l'eau de mer a intensifié le problème de l'évacuation de la saumure, soulevant des préoccupations environnementales en raison de sa forte salinité et de sa charge chimique. Cette étude explore une voie de valorisation durable en couplant des données industrielles issues de l'usine de dessalement UTE de Skikda, en Algérie, avec un modèle numérique d'électrolyse asymétrique à écart nul pour la récupération de produits de valeur, notamment l'hydrogène (H_2) et les ions hydroxyde (OH^-). Un outil de simulation basé sur MATLAB a été développé pour évaluer les performances de l'électrolyseur selon différents paramètres de fonctionnement, tels que la tension, la température, l'accumulation de bulles de gaz, le rendement faradique et l'effet du facteur de capture des hydroxydes. La courbe de polarisation a démontré que l'activation de l'anode améliore significativement l'efficacité du système, réduisant la résistance interne de près de 70 % et augmentant les performances jusqu'à 65 %. L'évaluation des performances a montré une forte concordance entre les résultats de simulation et les données expérimentales pour la production d'hydrogène, tandis que des écarts plus importants ont été observés dans l'évolution du courant au fil du temps, principalement dus à l'accumulation de bulles de gaz et aux hypothèses simplifiées du modèle. L'étude paramétrique a révélé qu'une augmentation de la température réduit la résistance cathodique de 46 % et augmente la production d'H_2 de plus de 60 %. De même, une couverture en bulles supérieure à 30 % augmente fortement les pertes ohmiques, tandis qu'un facteur de capture des hydroxydes supérieur à 0,9 nuit considérablement à la conductivité et à la production de gaz. Les écarts entre les données simulées et expérimentales mettent en évidence l'impact de phénomènes réels tels que la couverture par les bulles et les réactions secondaires, soulignant la nécessité de modèles plus complets et dynamiques.

Mots-clés : Osmose inverse (RO), valorisation de la saumure, cellule à écart nul, simulation MATLAB.

List of abbreviations

µmol/s	Micromole per second (unit of molar flow rate)
A/cm²	Ampere per square centimeter (current density)
CFD	Computational Fluid Dynamics
Cl_2	Chlorine gas
Eq.	Equation
F_{eff}	Faradaic Efficiency
H_2	Hydrogen gas
$HClO^-$	Hypochlorite ion
HER	Hydrogen Evolution Reaction
I	Current
MATLAB	Matrix Laboratory (numerical computing software)
NaCl	Sodium Chloride
NaOH	Sodium Hydroxide
OER	Oxygen Evolution Reaction
OH^-	Hydroxide ion
pH	Power of Hydrogen (measure of acidity/basicity)
RO	Reverse Osmosis
T	Temperature (Kelvin)
UTE	Unidad Técnica Especializada (Desaladora Station in Skikda)
V	Voltage
α	Fraction of hydroxide ions adsorbed on the electrode surface
Ω	Ohm (unit of electrical resistance)
ε	Bubble coverage factor

List of figures

List of Tables

Table of content

General Introduction

As global freshwater reserves face mounting pressure from population growth, industrialization, and climate change, seawater desalination has become an essential technology for ensuring water security. This is particularly true in arid and semi-arid regions such as Algeria, where freshwater resources are scarce and unevenly distributed, with per capita availability below 500 m^3/year a critical threshold for water stress[1]. Among the various desalination technologies, reverse osmosis (RO) has emerged as the most widely adopted due to its relatively low energy consumption and modular design[1]. However, despite its advantages, the process presents a significant environmental challenge: the generation of concentrated brine, which is typically discharged into the sea, posing risks to marine ecosystems due to its high salinity and chemical additives [1], [2].

The UTE Desaladora plant in Skikda, Algeria, exemplifies large-scale RO desalination infrastructure, with a nominal production capacity of 100,000 m^3/day. It supplies drinking water to nearby communities and supports industrial activities at the Skikda petrochemical complex. Operating at an average recovery rate of 47%, the plant transforms seawater into potable water while generating a brine stream enriched in sodium, chloride, and other dissolved ions. Current brine disposal practices involve direct discharge into the marine environment, which can elevate local salinity levels and disrupt benthic habitats. Although regulations exist to limit ecological harm, these measures often fail to address long-term impacts in shallow or poorly circulated coastal zones.

Electrochemical technologies, particularly membrane-based electrolysis, offer promising routes for brine valorization by extracting valuable compounds such as hydrogen gas (H_2), chlorine (Cl_2), sodium hydroxide (NaOH), and hypochlorite ions (ClO^-) [3] [4]. Zero-gap electrolyzer designs, which minimize interelectrode distance to reduce ohmic losses, are critical for improving energy efficiency in these systems[5][6][7]. For instance, Phillips and Dunnill demonstrated that zero-gap configurations in alkaline electrolysis enhance current density distribution and reduce voltage losses by up to 20% compared to conventional setups1. Similarly, de Groot and Vreman quantified the ohmic resistance reduction achieved using Zirfon diaphragms in zero-gap alkaline electrolyzers, highlighting their suitability for saline feedstock electrolysis[6]. These compounds have high commercial value and can potentially offset the operational costs of desalination[8]. Coupling brine electrolysis with renewable energy sources, such as solar photovoltaics, aligns with green chemistry principles and circular economy objectives, reducing carbon emissions and transforming desalination plants into integrated water-energy-resource recovery hubs[1].

This work explores the potential of electrochemical brine valorization using an asymmetric zero-gap electrolyzer. Field data from the UTE Desaladora plant informed the development of a MATLAB-based simulation model that captures electrochemical behavior under varying

operating conditions, including overpotentials, gas production rates, and bubble coverage effects. The model integrates multi-physics approaches to resolve transport phenomena and electrochemical kinetics, building on methodologies validated by Henao et al. for alkaline electrolyzers[9]. The originality of the work lies in combining operational desalination plant data with pilot-scale electrolyzer modeling, enabling a realistic assessment of technical feasibility and environmental benefits[9]. By employing a flexible zero-gap cell design, the system supports experimentation with diverse electrode materials and operating modes, facilitating continuous process optimization[5][7]

1 Chapter 1: Practical training at industry

1.1 Introduction

The UTE Desaladora plant in Skikda, Algeria, is a large-scale reverse osmosis (RO) facility producing up to 100,000 m^3 of potable water per day. While crucial for meeting regional water demand, particularly for the adjacent petrochemical complex, the process operates at a 47% conversion rate generating a significant volume of highly concentrated brine (50–75 g/L), which poses serious environmental challenges.

Although the internship was not centered on brine valorization which remain unaddressed challenge for the plant, it provided essential technical exposure to the RO system and enabled the collection of real operational data. These data, including flow rates, pressures, salinity, and pH, were critical inputs for the independent development of a mathematical model tailored to simulate brine electrolysis under realistic conditions.

In this context, the training served as a foundation for constructing a predictive numerical model for the chlor-alkali electrolysis process. Using MATLAB, simulations were conducted to evaluate key parameters such as current density, cell performance, and gas production efficiency. This approach, based on non-linear modeling and parametric analysis, aims to explore brine electrolysis as a sustainable pathway for converting waste into valuable chemicals like ClO- and NaOH, adapted to the specific constraints of RO plants such as UTE Desaladora.

1.2 Problematic and motivation

As Algeria faces growing freshwater scarcity, seawater desalination via reverse osmosis (RO) has become essential. Yet, RO presents two major sustainability challenges: high energy consumption typically from fossil fuels, and the discharge of hypersaline brine, which threatens marine ecosystems. This internship aimed to explore how these drawbacks can be addressed by integrating renewable energy sources and converting brine into value-added chemicals. Specifically, it served as a platform to assess the feasibility of hydrogen production through solar-powered electrolysis and the recovery of useful by-products like HClO- and NaOH.

A strong focus was placed on modeling and simulation to support this integration. By numerically analyzing parameters such as brine concentration, solar input, cell voltage, and temperature, the goal was to identify optimal conditions for continuous, efficient, and low-impact operation. This directly supports the objectives of my graduation project, which centers on the development and validation of predictive models for sustainable brine valorization under realistic operating conditions.

1.3 Training objectives and achivements

The main objective of the training at the UTE Desaladora station was to apply theoretical knowledge of water treatment in a real-world desalination plant and to collect operational data to support modeling efforts in a graduation project. Throughout the internship, the work focused on three key areas. First, data acquisition was carried out by monitoring critical parameters such as pressure, flow rate, conductivity, and temperature across the pre-treatment, reverse osmosis, and post-treatment units. Sampling campaigns targeted both permeate and rejected brine at various process stages. Second, laboratory characterization was conducted through physical-chemical analyses (pH, salinity, conductivity, turbidity, ion content) to assess the quality of both product water and concentrated brine. This allowed for the validation of plant performance against standard limits and facilitated early detection performance deviation. Finally, the numerical relevance of the training was emphasized, as the collected data provided a real baseline for simulating brine electrolysis in MATLAB. Parameters such as brine salinity, temperature, and pH were directly fed into the development and calibration of predictive models for H_2, Cl_2, and OH- generation. This ensured that the modeling phase was grounded in realistic process conditions, reducing guesswork and laboratory testing time.

1.4 Conclusion

This industrial training at the UTE Desaladora station provided valuable insights into the practical operation of reverse osmosis and the management of brine waste. Beyond hands-on experience with water treatment processes, the internship was instrumental in collecting real operational data such as: flow rates, pH, salinity, conductivity; which directly supported the development and validation of simulation models for brine valorization. The data collected enabled a more accurate representation of real conditions in MATLAB, improving the reliability of the simulations aimed at optimizing the recovery of Hydrogen and NaOH. This synergy between field data and computational modeling laid a solid foundation for advancing the experimental and numerical components of the graduation project.

2 Chapter 2: State of the art and bibliographic research

a. Numerical Modeling of Zero-Gap Electrolyzers: Historical Perspective

The numerical modeling of electrolyzers has long been a crucial tool in understanding and optimizing electrochemical processes. Historically, early efforts in modeling electrolysis focused on empirical relationships and basic current-voltage analyses to assess cell performance, relying on bulk parameters like Faraday's laws and ohmic losses[6]. These models were limited in scope, often restricted to steady-state analyses, with minimal consideration for the intricate interplay between electrochemical kinetics, thermal effects, and mass transport. With the advent of computational power and deeper theoretical understanding, modeling evolved to encompass more detailed physics-based representations, especially for advanced systems like zero-gap electrolyzers.

Zero-gap electrolyzers—characterized by the minimal spacing between electrodes separated only by an ion-conducting membrane—have gained significant attention for their compact design, high energy efficiency, and scalability in hydrogen production and brine valorization applications [5]. Initially, modeling in this area adapted approaches from broader classes of alkaline or PEM electrolyzers. However, the specific configuration of zero-gap systems introduces unique challenges: thin-layer transport phenomena, localized bubble formation, pressure gradients, and interfacial reactions occurring at microscale distances (typically <2 mm) [5]. These complexities, including significant contributions from ohmic resistance within the narrow gap and diaphragm [6], necessitated the development of more sophisticated numerical approaches that account for spatial and temporal variations. Modern modeling must accurately characterize these losses and dynamic behavior to predict performance under varied operating conditions, moving beyond simple empirical I–V curves [7].

b. Numerical Modeling of Zero-Gap Electrolyzers: Evolution

The transition from steady-state to dynamic and multi-physics models marked a significant milestone. In particular, proton exchange membrane (PEM) electrolyzer modeling has served as a foundation, given the structural similarity with zero-gap systems. The work by Corbeltaldo et al. (2017)[10], for instance, presents a zero-dimensional dynamic model for PEM electrolyzers that includes activation, ohmic, and concentration overpotentials, along with parasitic losses and transient thermal dynamics. Their approach integrates the electrochemical and thermal response to input fluctuations, making it particularly relevant for coupling with intermittent renewable energy sources. Such a framework is useful for zero-gap systems but must be further adapted to account for the extremely reduced inter-electrode distance and the enhanced role of capillary and bubble-induced resistances.

Simultaneously, process-level models—such as the one discussed by Shulaeva et al. (2017)[11]—have explored the industrial-scale electrolysis of brine for co-production of chlorine, hydrogen, and sodium hydroxide. These models calculate ion transport through the electrolyte under the influence of electrochemical potential, including considerations of viscous drag and solvation effects. While not zero-gap specific, these models highlight the need to incorporate fluid dynamics and physicochemical interactions between ionic species and the electrolyte medium. Moreover, the insights regarding temperature and inter-electrode distance on process efficiency directly translate into the design considerations of zero-gap systems, where temperature can alter electrolyte viscosity and hence the conductivity and rate of gas evolution.

c. Numerical Modeling of Zero-Gap Electrolyzers: Research Directions

Despite important developments in the modeling of water electrolysis systems, significant gaps persist in the literature when it comes to zero-gap electrolyzers operated under dynamic or continuous conditions. Most conventional models simplify geometries excessively or overlook critical variations such as gas bubble accumulation, electrode morphology, and local pH gradients, which are particularly relevant in foam-based or porous electrodes typically used in these systems[12]. Studies have shown that idealized assumptions about electrode surfaces and homogenous fields lead to deviations between simulation and experimental performance, especially under high current densities or fluctuating conditions[13]. Moreover, limited attention has been given to systems using brine or impure feedstocks, which introduce challenges like ion competition, and scale formation that are not well captured in simplified models[14].

Recent research suggests a growing interest in multi-scale and dynamic modeling approaches that combine electrochemical kinetics with transport phenomena across the electrode–electrolyte–membrane interfaces[15]. For example, computational fluid dynamics (CFD) and coupled transport models have been used to resolve gas evolution, local overpotentials, and resistive losses across different configurations[15]. These studies highlight the importance of capturing non-uniform current distribution and bubble-induced mass transfer limitations, especially in zero-gap geometries, where small distances between electrodes amplify such effects[12]. However, the integration of real-time operational variability—such as fluctuations in feed composition, temperature, or voltage—into predictive models remains limited[12]. Addressing this gap is crucial for advancing Power-to-X strategies and for enabling more robust, scalable, and energy-efficient hydrogen production from variable sources, particularly using low-cost and saline water electrolytes[12], [14].

3 Chapter 3: Proposed solution

3.1 Introduction

The numerical model is developed to simulate the performance of the asymmetric zero-gap electrolysis system used in the valorization of brine through hydrogen, hydroxide and hypochlorous ions production. The primary objective of this work is to capture the interplay between electrochemical kinetics, materials dynamic behaviour, and system configuration under different operating conditions (voltage, temperature, bubble coverage, faradic efficiency, current division factor, captured hydroxide percentage and time). The proposed model incorporates all the electrolyzer's components namely cathode, anode and diaphragm providing an accurate representation of the cell's behavior.

This numerical framework allows us to evaluate the influence of key parameters such as cell's temperature, bubble coverage, and faradic efficiency on hydrogen yield and energy efficiency. By comparing outputs at 6V, the study aims to provide a comprehensive study and a mechanistic analysis of the electrolysis process.

3.2 Numerical model

This section describes the theoretical modeling framework and physical principles used to analyze the performance of the zero-gap electrolyzer system. The model incorporates all relevant electrochemical, physical, and thermodynamic phenomena governing the response of the electrlyzer.

a. Cell geometry and material constants

The electrochemical cell is composed of two porous electrodes, namely nickel foam for the cathode and carbon foam for the anode, in addition to Zirconium oxide-based porous diaphragm acting as a separator. The effective geometric surface areas of the electrodes account for porosity and are given by Eqs 1 and 2:

$$S_a^{eff} = S_a(1-\varepsilon) \quad (1)$$

$$S_c^{eff} = S_c(1-\varepsilon) \quad (2)$$

where ε is the bubble coverage.

The anode is made of porous carbon foam (electronic conductor), while the cathode is composed of porous nickel foam. The Zirfon diaphragm, being a porous ceramic-polymer

composite, allows ionic conduction while minimizing gas crossover, making it well-suited for alkaline and neutral media. All the characteristics are indicated in Table.1:

Table 1 Characteristics of the used materials

	Diaphragm	Carbone foam	Nickel foam
Porosity (ε)	0.55	0.95	0.95
Tortuosity (τ)	2.04	1.5	1.5
Dimensions (Thickness(cm)×S(cm²))	0.05×13	0.3×13	0.1×13

The electrical conductivity of the solid materials used in the cell, such as nickel foam and carbon foam, is temperature-dependent. The effective conductivity of nickel foam is first corrected for temperature and then expressed using the Gibson-Ashby model, which accounts for its porosity and tortuosity. The temperature-adjusted conductivity of nickel is given by Eq.3:

$$\sigma_{Ni} = \frac{\sigma_{Ni}^{0}}{1 + \alpha_T (T - 293)} \tag{3}$$

Here, $\sigma_{\mathrm{Ni}}^{0} = 1.43 \times 10^{4}$ S/cm [16]; is the reference conductivity at 293 K and $\alpha_T = 5.866 \times 10^{-3}$ [17] is the temperature coefficient. The effective conductivity of the nickel foam, accounting for its porous structure, is then:

$$\sigma_{Ni}foam = \sigma_{\mathrm{Ni}}^{0}(1 - \varepsilon)^{\tau} \tag{4}$$

Similarly, the conductivity of the carbon foam, used in some experimental configurations, is modeled as an exponential function of temperature based on empirical data:

$$\sigma_{Cfoam} = 60 \cdot \exp\left(-\frac{17000}{R}\left(\frac{1}{T} - \frac{1}{293}\right)\right) \tag{5}$$

The ionic conductivity of the electrolytes in the anode and cathode compartments varies depending on composition and temperature. For the catholyte, the conductivity evolves with time due to the accumulation of hydroxide ions produced during electrolysis and is calculated using the Nernst-Einstein relation:

$$\sigma_{ions} = \frac{F^2}{RT} \sum_{i} Z_i^2 D_i C_i \tag{6}$$

With Z_i is the ionic charge, D_i the diffusion coefficient (in m^2/s) of ion i in water, and C_i is the ion concentration (in $\mathrm{mol/m}^3$).

For the catholyte, the conductivity is considered the sum of two contributions: the constant baseline conductivity of pure water and the NaOH contribution, which depends on the hydroxide ion concentration. Considering the dynamic evolution of the composition of the catholyte, Eq.7 is written as:

$$\sigma_{catholyte} = \sigma_{H_2O} + \sigma_{NaOH}(cathode) \quad (7)$$

$\sigma_{H_2O} = 24.2 \times 10^{-4}\ S/m$ is treated as a constant, while the NaOH conductivity is modeled as:

$$\sigma_{NaOH}(cathode) = (248.7 + 0.928T)\left(C_{HO^-_{free}}\right)^{0.922} \quad (8)$$

Since the anolyte in this study contains a dilute NaCl solution at quasi-constant concentration and pH ≈ 9, the contribution from NaOH is considered negligible, making $\sigma_{anolyte}$ effectively constant following Eq.9:

$$\sigma_{anolyte} = \sigma_{\mathrm{NaCl}} + \sigma_{NaOH}(anode) \approx \sigma_{\mathrm{NaCl}} \quad (9)$$

The conductivity of NaCl is modeled using Eq.10:

$$\sigma_{\mathrm{NaCl}} = \left(\frac{F^2}{R \cdot T_{\mathrm{cell}}}\right) \cdot \left(C_{\mathrm{NaCl}} \cdot (D_{\mathrm{Na}} + D_{\mathrm{Cl}})\right) \quad (10)$$

Where $F = 96485\ C/mol$ is the Faraday constant, and $C_{\mathrm{NaCl}} = 70 g/L$ is the NaCl concentration. The diffusion coefficients of Na^+ and Cl^- in water are temperature-dependent and given by Eqs. 11, 12:

$$D_{\mathrm{Na}} = D_{0,\mathrm{Na}} \cdot \exp\left(\frac{-20000}{R \cdot T_{\mathrm{cell}}}\right) \quad (11)$$

$$D_{Cl} = D_{0,Cl} \cdot \exp\left(\frac{-18500}{R \cdot T_{\mathrm{cell}}}\right) \quad (12)$$

With: $D_{0,\mathrm{Na}} = 4.279 \times 10^{-6} m^2/s$ and $D_{0,\mathrm{Cl}} = 3.56 \times 10^{-6} m^2/s$.

The Zirfon diaphragm separating the two compartments is treated as a porous medium, and its effective conductivity is calculated using a harmonic mean expression between the conductivities of the anolyte and catholyte as mentioned in Eq. 13, with ε_{dia} and τ_{dia} from Table 1:

$$\sigma_{dia} = \frac{\sigma_{anolyte} - \sigma_{catholyte}}{ln\left(\frac{\sigma_{anolyte}}{\sigma_{catholyte}}\right)} \frac{\varepsilon_{dia}}{\tau_{dia}} \quad (13)$$

The total ohmic resistance of the cell consists of three components: the resistance of the anode, the cathode, and the diaphragm. Each electrode's resistance is the sum of the electronic

resistance through the solid matrix and the ionic resistance through the electrolyte-filled pores. The membrane resistance is defined as :

$$R_{dia} = \frac{L_{dia}}{\sigma_{dia} S_{dia}} \tag{14}$$

The anodic resistance is modeled by:

$$R_a = \frac{L_a}{\sigma_{Cfoam} S_a^{eff}} + \frac{L_a}{\sigma_{anolyte} \frac{\varepsilon_a}{\tau_a} S_a^{eff}} \tag{15}$$

The cathodic resistance is given by:

$$R_c = \frac{L_c}{\sigma_{Ni}foam S_c^{eff}} + \frac{L_c}{\sigma_{catholyte} \frac{\varepsilon_c}{\tau_c} S_c^{eff}} \tag{16}$$

The electrode thicknesses are denoted L_a, L_c, and the diaphragm thickness L_{dia}.

The first term in each resistance expression represents the electronic resistance through the solid phase, while the second accounts for the ionic resistance through the electrolyte-filled pores. The resistance dynamic over time due to changes in electrolyte concentration and current density, affecting the overall ohmic losses during electrolysis.

b. Electrochemical overpotentials and cell performance

The total cell voltage consists of the sum of the different voltages according to Eq.17 [18]:

$$U_{cell} = E_{rev} + U_{Conc} + U_{act} + U_{Ohm} \tag{17}$$

The first term E_{rev} is the reversible voltage at the specific temperature T and atmospheric pressure, representing is the minimum voltage necessary for the electrolysis reaction to start and is given by Eq.18 [19]:

$$E_{rev,T} = 1.5184 - 1.5423 \times 10^{-3} T + 9.524 \times 10^{-5} T ln(T) + 9.84 \times 10^{-8} T^2 \tag{18}$$

U_{act} is the sum of the anodic and cathodic activation overpotentials caused by the kinetics at the electrodes. The anodic and cathodic activation voltages can be obtained using the Tafel equation as shown in Eqs.19 and 20:

$$U_{act,a} = \frac{RT}{\alpha_a \cdot 4F} \ln\left(\frac{I}{S_a^{eff} J_{0,a}}\right) \tag{19}$$

$$U_{act,c} = \frac{RT}{\alpha_c \cdot 2F} \ln\left(\frac{I}{S_c^{eff} J_{0,c}}\right) \quad (20)$$

$$U_{act} = U_{act,a} + U_{act,c} \quad (21)$$

j_{0_a} and j_{0_c} refer to the non-activated anode Eq.22 and activated anode Eq.22' and cathodic exchange current densities Eq.23, respectively, which constitute the rate at which electrons are exchanged between the electrode and the electrolyte at equilibrium, i.e., with zero overpotential. A higher exchange current density means that the electrodes facilitate fast charge transfer and rapid electron and ion exchange [20], [21], while α_a=α_c=0.5 are the charge transfer coefficients.

$$J_{0,a} = 6.06 \times 10^{-5} \cdot \exp\left(\frac{-17000}{R}\left(\frac{1}{T} - \frac{1}{293}\right)\right) \quad (22)$$

$$J_{0,a} = 0.0164 \cdot \exp\left(\frac{-17000}{R}\left(\frac{1}{T} - \frac{1}{293}\right)\right) \quad (22)$$

$$J_{0,c} = 4.79 \times 10^{-5} \cdot \exp\left(\frac{-20000}{R}\left(\frac{1}{T} - \frac{1}{293}\right)\right) \quad (23)$$

The ohmic overpotential U_{Ohm}, is caused by the ohmic losses during the electrolysis of water, due to the formation of the gas bubble, and the electrical energy dissipated and the ions passing through the electrolyte. The ohmic voltage is determined by the ohmic resistance according to the Ohm's law as shown in Eq.24:

$$U_{ohm} = R_{ohm}.I \quad (24)$$

The ohmic resistance R_{ohm} is the sum of the resistance of the electrodes (anode and cathode) and the resistance of the diaphragm, as shown in Eq.25.

$$R_{ohm} = R_a + R_c + R_{dia} \quad (25)$$

U_{conc} is the sum of the anodic and cathodic concentration overpotentials, $U_{conc,a}, U_{conc,c}$, arise from the accumulation or depletion of species near the electrode surfaces when mass transport cannot keep up with the reaction rate [22]. These overpotentials can be calculated using the following expressions:

$$U_{conc,a} = \frac{RT}{4F} \cdot \left[-\ln\left(1 - \frac{I}{I_{lim,a}}\right)\right] \quad (26)$$

$$U_{conc,c} = \frac{RT}{2F} \cdot \left[-\ln\left(1 - \frac{I}{I_{lim,c}}\right)\right] \quad (27)$$

$$U_{conc} = U_{conc,a} + U_{conc,c} \quad (28)$$

The limiting current densities $I_{lim,a}, I_{lim,c}$ represent the maximum current that can be sustained by the mass transport of reactants to the electrode surface, and are given by:

$$I_{lim,a} = \frac{F \cdot S_a^{eff} \cdot D_a \cdot C_a}{\delta_a} \quad (29)$$

$$I_{lim,c} = \frac{2 \cdot F \cdot S_c^{eff} \cdot D_c \cdot C_c}{\delta_c} \quad (30)$$

Water is considered as the sole reactant in the cathode compartment, and though the limiting reactant in the anode compartment is plausibly HO-, water is also the limiting species because of the rapid depletion of hydroxide ions in the anodic compartment at pH 9.

The diffusion coefficients D_a, D_c for the anode and cathode compartments, respectively, are expressed as temperature-dependent functions:

$$D_a = D_{0a} \cdot \exp\left(\frac{-20000}{RT}\right) \quad (31)$$

$$D_c = D_{0c} \cdot \exp\left(\frac{-20000}{RT}\right) \quad (32)$$

Where $D_{0a} = D_{0c} = 7.4 \times 10^{-2}\ \mathrm{cm^2/s}$ is the pre-exponential factor corresponding to the auto-diffusion of water. The concentrations of the limiting species are considered constant and equal on both sides: $C_a = C_c = 55500\ mol/m^3$. The diffusion layer thicknesses in the zero-gap electrolyzer are estimated as: $\delta_a = \delta_c = 10^{-5}\ m$.

c. Flow rates and pH evolution

i. Main electrochemical reactions

At the cathode, water is reduced to produce hydrogen gas and hydroxide ions:

$$2H_2O + 2\,e^- \rightarrow H_2 + 2OH^- \quad (33)$$

Sodium ions transported by the diaphragm then associate with hydroxide to form sodium hydroxide:

$$2Na^+ + 2\,OH^- \rightarrow 2\,NaOH \quad (34)$$

At the anode, depending on the brine composition and operating conditions, oxygen gas is evolved:

$$2\,H_2O \rightarrow 4\,H^+ + 4\,e^- + O_2 \quad (35)$$

With possible chlorine gas evolution:

$$2\,Cl^- \rightarrow Cl_2 + 2\,e^- \quad (36)$$

ii. Molar Flow Rates

The molar flow rates of the product gases (mol/s) and ions are derived from Faraday's law, accounting for the faradaic efficiency η_F:

$$\dot{n}_{H_2} = \frac{I}{2F} \cdot \eta_F \tag{37}$$

$$\dot{n}_{O_2} = \beta \cdot \frac{I}{4F} \cdot \eta_F \tag{38}$$

$$\dot{n}_{Cl_2} = (1-\beta) \cdot \frac{I}{2F} \cdot \eta_F \tag{39}$$

$$\dot{n}_{Na^+} = (1-\beta) \cdot \frac{I}{F} \cdot \eta_F \tag{40}$$

$$\dot{n}_{HO^-} = 2 \cdot \dot{n}_{H_2} \tag{41}$$

$$\dot{n}_{HO^-_{free}} = 2 \cdot \dot{n}_{H_2}(1-\alpha) \tag{42}$$

Where β is a selectivity parameter between oxygen and chlorine evolution at the anode, and α is the fraction of hydroxide ions adsorbed on the electrode surface.

iii. Volumetric Flow Rate

Assuming ideal gas behavior, the volumetric flow rate of hydrogen is calculated as:

$$\dot{V}_{H_2} = \dot{n}_{H_2} \frac{RT}{P} \tag{43}$$

iv. Cathodic pH Evolution

Assuming that hydroxide ions accumulate in the cathodic compartment, the concentration of free hydroxide evolves as:

$$C_{HO^-_{free}} = \frac{2\,\dot{n}_{H_2}(1-\alpha)\,\Delta t}{V_{circuit}} \tag{44}$$

$$C_{OH^-}^{init} = 10^{-8.5} \tag{45}$$

$$pH_{cathode} = 14 + \log_{10}\left(C_{OH^-}^{init} + \frac{2\,\dot{n}_{H_2}(1-ads)\,\Delta t}{V_{circuit}}\right) \tag{46}$$

Where $V_{circuit}$ is the working volume of the cathodic compartment, and Δt is the duration of electrolysis.

d. Power Consumption

The power consumed by the cell is simply given by:

$$P_{cell} = I \cdot U_{cell} \tag{47}$$

Where I is the instantaneous current (A) and U_{cell} is the total cell voltage including all overpotentials

3.3 Numerical procedure

The numerical procedure followed in this study aims to characterize the behavior and performance of a developed asymmetric zero-gap electrolyzer through multiparametric simulation. This includes the modeling of polarization curves, gas evolution dynamics, and physicochemical properties under varying operating conditions. The procedure was structured in several steps to analyze the dynamic regime, enabling the prediction of current output, targeted products evolution, and components efficiency. The study also considers the influence of electrode material, focusing on the effect of using activated carbon foam with $Ni(OH)_2$ instead of the conventional one.

The first stage involved the simulation of the polarization curve over a wide voltage range (2–18 V) with a step size of 2 V. For each voltage, the maximum current density (I_{max}) was recorded to map the cell's voltage-current behavior. Subsequently, the system's performance was evaluated at 6 V. These simulations were used to determine the bubble coverage factor (e_{bubble}) that yields the closest simulated mean current (I_{moy}) to the values obtained experimentally, under the assumption of a 100% Faradaic efficiency.

A detailed parametric analysis followed, investigating the effects of five key variables: cell temperature (T_{cell}), cell voltage (U_{cell}), bubble coverage (ε_{bubble}), hydroxid capture factor (α), and Faradaic efficiency (F_{eff}). This phase helped identify the sensitivity of each parameter on the cell's hydrogen output, overpotential, and ohmic losses and construct a comprehensive view of the response of the electrolyser based on mechanisms.

Finally, the entire simulation workflow was repeated with a modified configuration where the anode electrode was activated by $Ni(OH)_2$. This allowed for the assessment of its impact on electrochemical performance, including conductivity, gas evolution, and overall cell efficiency. The resulting data serve as a comparative framework for future experimental validation and optimization.

Table 2 (appendix) summarizes the adopted parameters and their ranges used in the numerical simulations for the non-activated and activated anode.

4 Chapter 4: Results and discussion

4.1 Polarization curve

In order to characterize the performance of the systems, the current flowing through the electrolyzer was simulated as function of the applied potential to build the polarization curve. The results shown in Fig.1 indicate that the simulation closely matches the experimental data for the activated anode with a correlation coefficient exceeding 0.9969, demonstrating the reliability of the presented model. In contrast, some fluctuations were observed for the non-activated electrode a correlation coefficient exceeding 0.9686. These discrepancies can be attributed to the non-ideal nature of real operating conditions or to simplifications in the mathematical approaches. Nevertheless, the simulation remains generally reliable, reinforcing the validity of the adopted approach.

As the applied voltage increases, the polarization curve enters the ohmic region after overcoming the activation region, the current density then rises almost linearly with voltage. For the non-activated anode, a noticeable delay in the increase of current density is observed between 4 V and 10 V. This behavior suggests the influence of the current division factor β adding an additional resistive barrier. After 10 V, the current density increases more steeply, indicating that the system has overcome this limitation and begins to behave ideally. In contrast, the activated anode exhibits a steady and steeper slope throughout the ohmic region. The overall cell resistance shown in Eq.17 and inferred from the slope, is significantly lower for the activated anode approximately 2 Ω, compared to about 6.6 Ω for the non-activated cell. This corresponds to a reduction in resistance of nearly 70%, confirming the beneficial effect of surface activation on anode performance. At 20 V, the current density reaches 0.71 A/cm² for the activated anode, compared to only 0.43 A/cm² for the non-activated one, representing a 65% improvement in performance, closely matching the experimental results.

As expected, the activated anode exhibited a significant enhancement in performance. This improvement is attributed to the formation of active sites on the anodic surface that are more favorable for the oxygen evolution reaction[23]. Also, this modification significantly increases the anodic exchange current density according to Eq.22’ facilitating electron transfer and allowing current to flow more easily[23], [24]. As a result, the overpotential decreases, the cell operates more efficiently, and higher current densities can be sustained with less energy input[23].

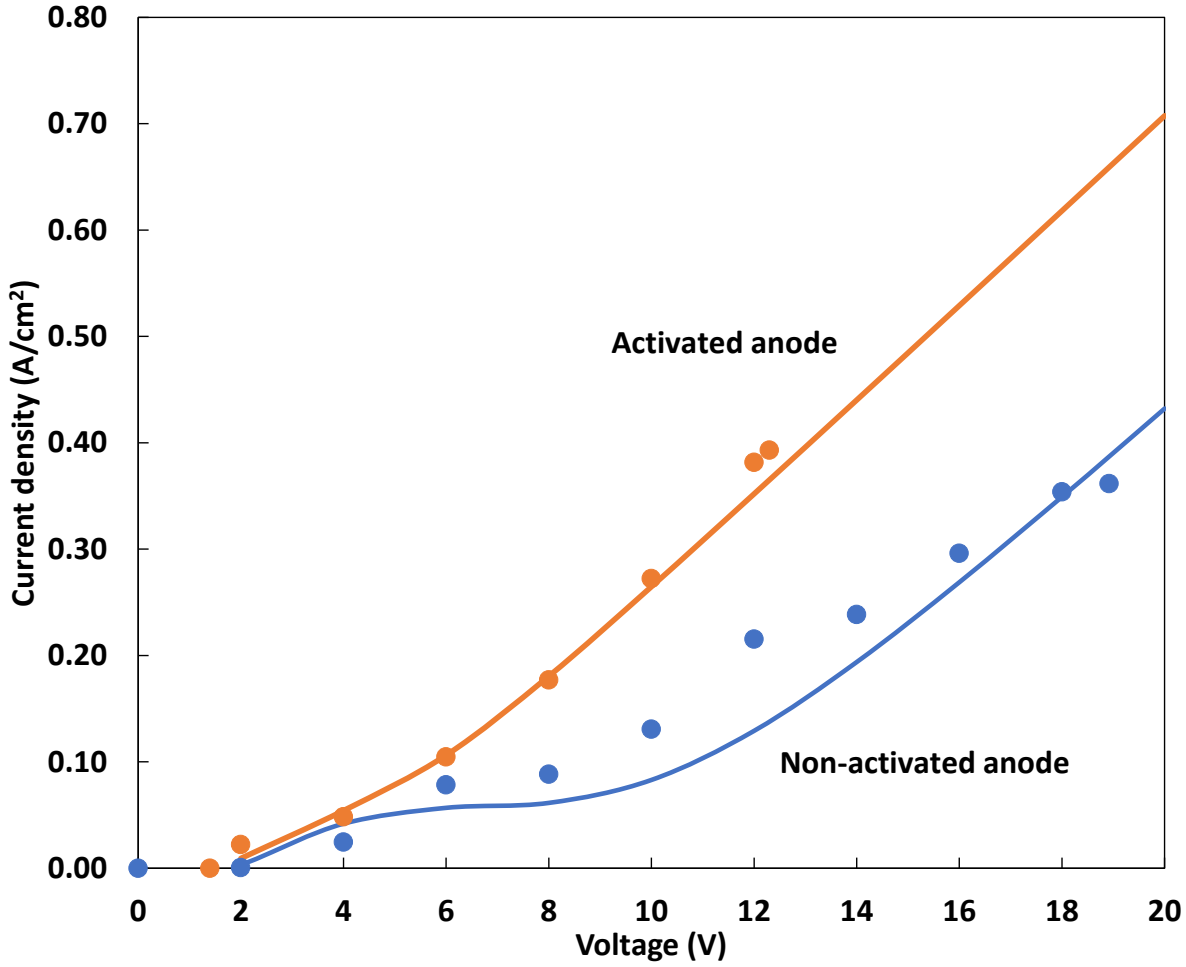

Figure 1 Polarization curves obtained through simulation (lines) and experiments (dots) for both activated and inactivated anodes.

4.2 Performance assessment

Fig.2 compares the temporal evolution of current for both the activated and non-activated anode configurations. In the experimental data, the current tends to decrease over time, whereas in the simulation, it increases progressively keeping the a near average current flow over time. This divergence stems from a fundamental assumption in the simulation model considering ideal operating conditions, particularly the absence of gas bubble accumulation due to presumed continuous electrolyte flow which is considered time independent. As a result, the model predicts that, over time, the pores of the diaphragm and electrode (particularly cathode) become increasingly filled with electrolyte, improving ionic conductivity. This leads to a gradual reduction in internal resistance and thus a rise in current density under a given operating voltage.

However, in real experimental conditions, several interfering phenomena occur. Firstly, gas bubbles, particularly hydrogen and oxygen, tend to accumulate within the electrode and dipahragm structures. These bubbles reduce the effective electrochemically active surface area as indicated in Eqs. 1, 2, and physically block electrolyte access to the porous matrix, thereby increasing local resistance. Secondly, by-products and reaction intermediates may adsorb onto the electrode surfaces over time, further increasing interfacial resistance and limiting charge transfer. These effects contribute to the observed decline in current during the experimental runs. In the following section, we will explore the effect of the bubble coverage percentage on the performance of the electrolyzer.

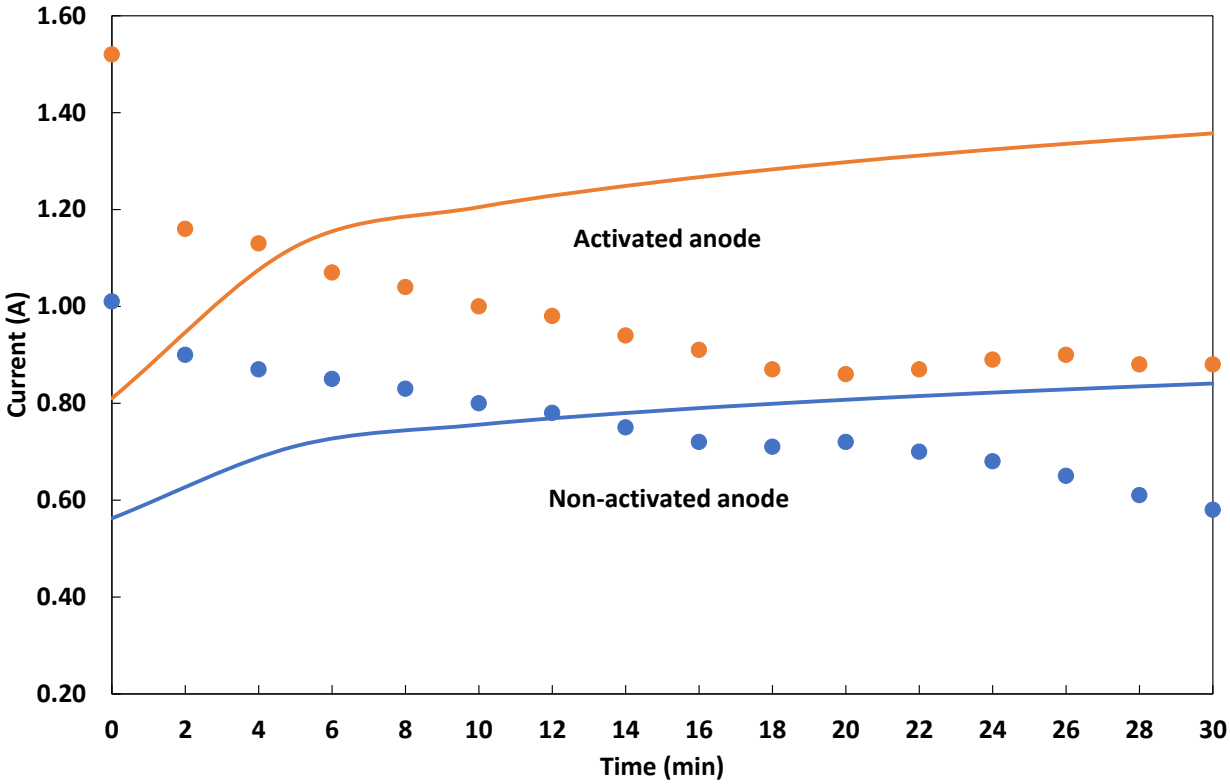

Figure 2 Evolution of current vs. time at 6 V obtained through simulation (lines) and experiments (dots) for both activated and inactivated anodes.

Fig.3 shows the evolution of free OH^- ions formed from the hydrogen evolution reaction (HER) in the cathodic compartment. OH^- is a targeted product in the brine electrolysis process for the production of NaOH, a key element in the proposed system. The graph clearly illustrates the impact of anode activation; the formation of OH^- ions is significantly enhanced when the anode is activated. This is attributed to improved ion exchange facilitated by the presence of active sites on the anodic surface, increasing consequently the flow of electrons[23].

At 6 V, the first 4 minutes correspond to a transient regime, during which the system stabilizes and the flow becomes more regular. Once stabilized, the activated anode achieves an average

OH^- production rate of approximately 11.6 µmol/s, compared to 7.37 µmol/s for the non-activated anode. This represents a 58% improvement in performance, reinforcing the effectiveness of the proposed solution.

When comparing simulation results to experimental data, it is observed that the experimentally measured free OH^- evolves roughly around the simulated values, with more pronounced fluctuations over time. Nonetheless, the free OH^- rate remains strictly lower than the total predicted production in the cathodic compartment according to the HER reaction. In real operating conditions, OH^- ions are more likely to undergo secondary reactions or recombine with impurities present in the electrolyte, such as divalent metal cations (e.g., Ca^{2+} or Mg^{2+}) which were not taken in consideration, or even recombining with protons H^+ that might locally generated[25]. These side reactions consume free OH^- ions, effectively reducing their measurable concentration. Additionally, limitations such as incomplete mixing since the continuous flow that enters is the only way to agitate, local pH variations, and separator crossover effects are typically not fully accounted for in the simulation, which assumes idealized and isolated conditions[26].

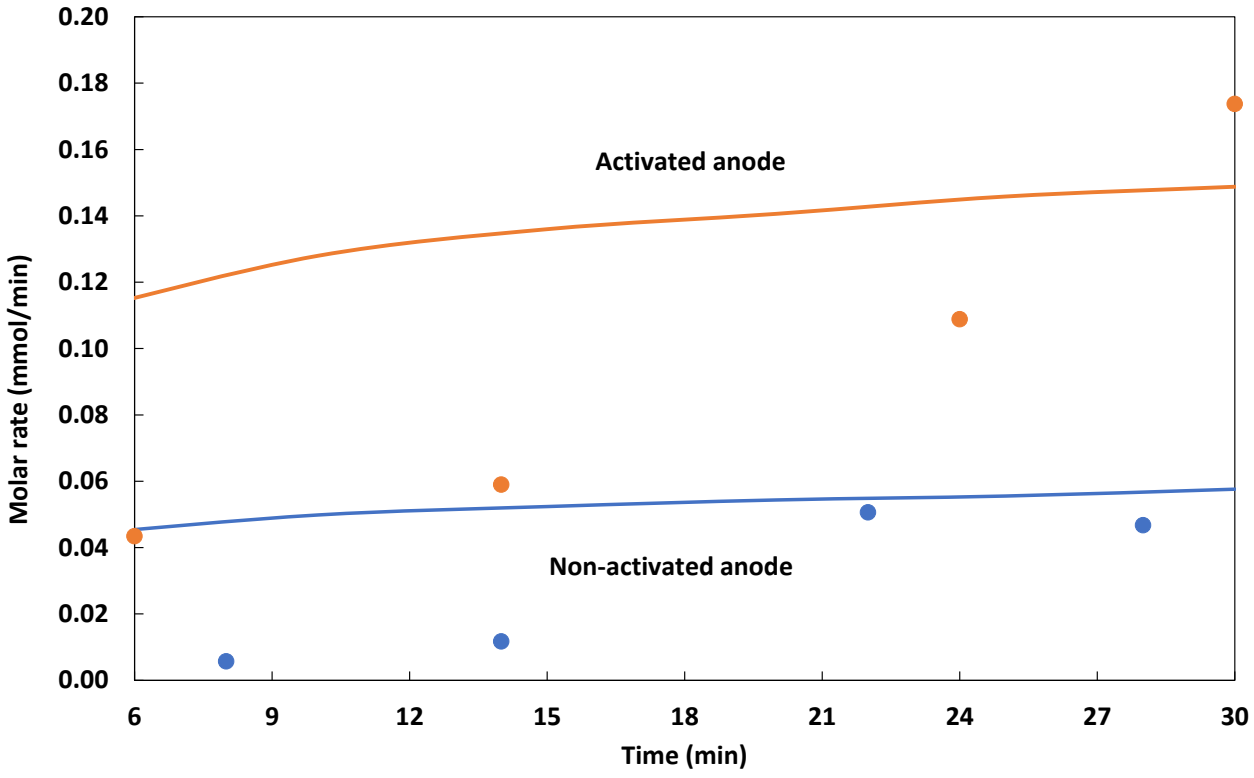

Figure 3 Evolution of the molar rate of cathodic free OH- vs. time obtained at 6 V through simulation (lines) and experiments (dots) for both activated and inactivated anodes.

Fig.4 presents a comparison between the average hydrogen flow rates obtained experimentally and those predicted by simulation, considering both activated and non-activated anode configurations. Hydrogen generation shows a strong agreement between simulation and experiment. This match can be attributed to the fact that hydrogen is directly produced by the hydrogen evolution reaction (HER) at the cathode and is less susceptible to parasitic or secondary reactions. As a result, the simulation accurately captures the system behavior, with a reliability estimated at around 80%. Moreover, anode activation significantly improves the overall electrolysis performance. By enhancing ionic conductivity and reducing charge-transfer resistance, it indirectly promotes higher hydrogen generation rates[27]. The activated anode leads to a 60% increase in hydrogen production compared to the non-activated configuration, making it a key factor in the efficiency of the proposed process.

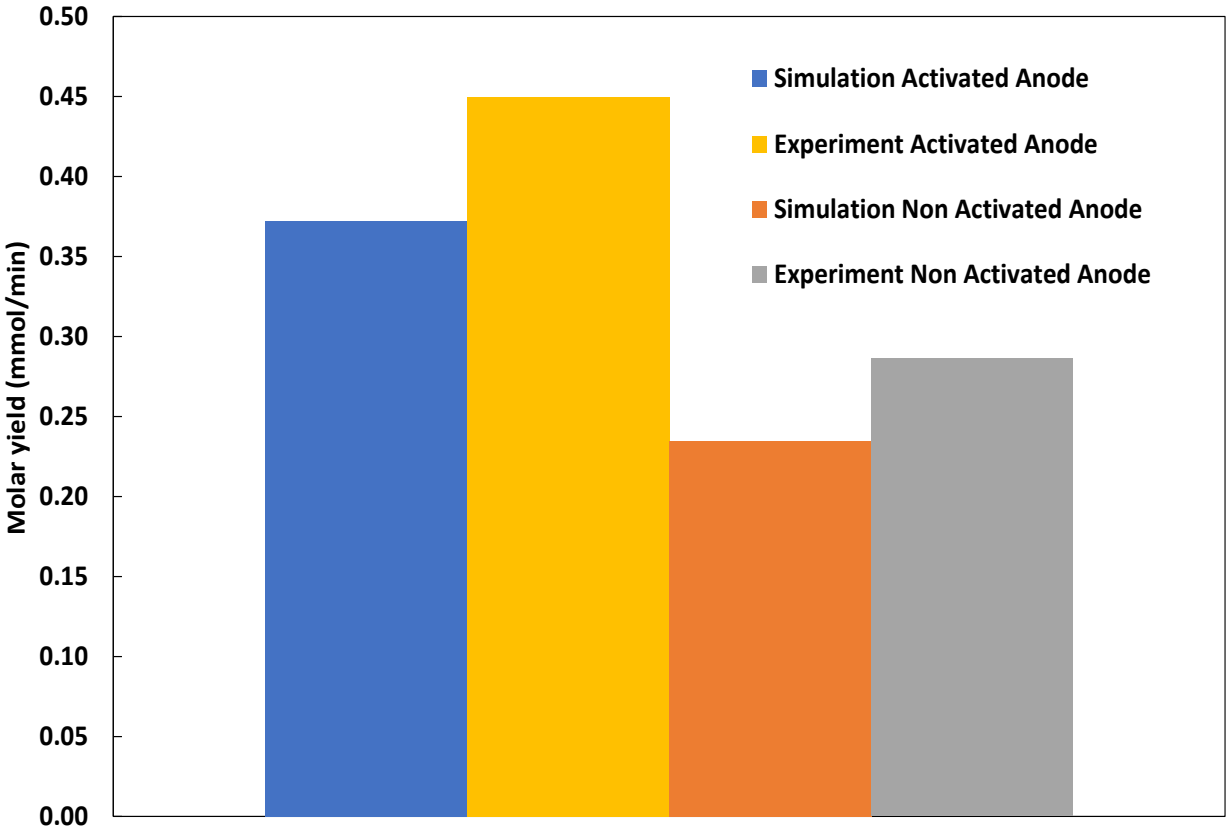

Figure 4 Average rates of H_2 obtained at 6 V through simulation and experiments for both activated and inactivated anodes.

The evolution of the different components of the ohmic resistance over time is evaluated as a key performance indicator to assess the effectiveness of anode activation and the dynamic performance of the electrolyzer as a function of time. Fig.5 illustrates the evolution of different resistance components, namely the diaphragm resistance as indicated Eq. 14, the anodic

resistance as shown in Eq. 15, and the cathodic resistance as illustrated in Eq. 16 for both activated and non-activated anode configurations.

Interestingly, anode activation leads to a noticeable decrease in cathode resistance over time. This is significant, as the cathode resistance accounts for nearly 80% of the total ohmic resistance in this case. This predominance stems from the zero-gap configuration operating without liquid electrolyte in the inter-electrode space, hence, the conductivity of the cathode, formed of a porous material (Nickel foam) is enhanced as long as conductive ions fill the pores. Initially, the cathodic compartment is only filled of reverse osmosis permeate with very low conductivity, inducing a high cathodic resistance. The formation of hydroxide ions through the HER reaction and the migration of Na^+ from the anodic to the cathodic compartment improves the overall cathodic conductivity and consequently reduces the resistance of the cathode. Anode activation indirectly enhances the cathode conductivity and cathodic ion exchange by creating more uniform, higher and stable current travelling across the cell, which advances the OER and HER, providing more available free OH^- and Na^+ ions to fill the pores of the cathode. A similar trend is observed for the diaphragm resistance, playing the role of the separator of both anodic and cathodic compartments, which also decreases with the activated anode. The diaphragm, being a porous structure, is affected by the ionic conductivity of the anolyte and catholyte. Though the anolyte composition is quasi-stable over time, the anolyte composition evolves from pure reverse osmosis permeate to an alkaline solution, and by the same effects mentioned previously, the anode activation improves the ionic conductivity of the catholyte, which improves the ionic conductivity throughout the pores of the diaphragm. In addition, the activation of the anode may improve water management and reduces local drying at the diaphragm interface. Conversely, a slight increase in anodic resistance is observed from 0.45 Ω to 0.57 Ω, corresponding to a 26% increase. This is a logical outcome of the activation process; while activation creates more active sites and improves reaction kinetics, it can also introduce a higher density of surface irregularities or oxide layers, slightly increasing the electronic resistance on the anodic side.

Despite the overall reduction in ohmic resistance by approximately 55%, the total ohmic losses remain constant at around 4.5 V. This indicates that the system can sustain higher current densities without increasing energy losses, which is a clear advantage. It suggests that the activation process enhances the current-carrying capacity of the cell while maintaining voltage efficiency an important benefit for scaling up and optimizing the electrolysis process.

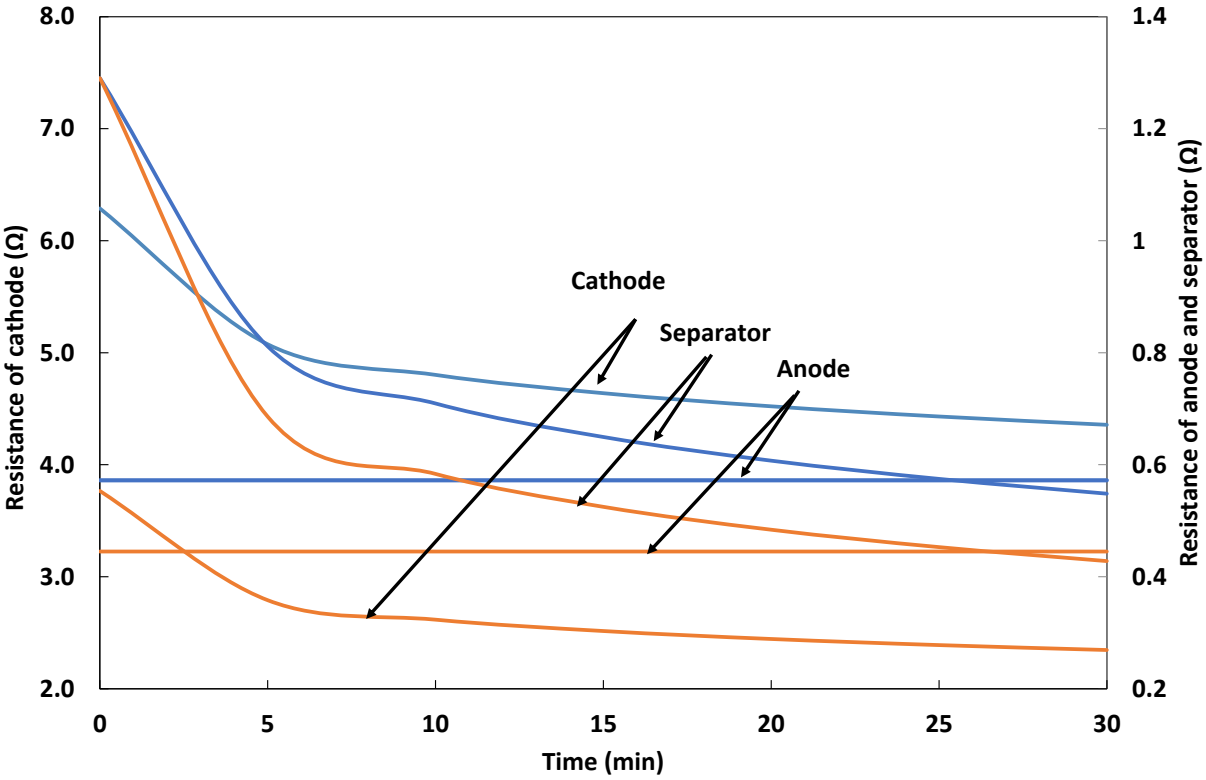

Figure 5 Evolution of the separator, anode and cathode resistances vs. time for both activated (orange) and inactivated (blue) anodes.

4.3 Parametric study

To assess the performance and efficiency of the electrochemical system configuration using activated vs. non-activated anodes under specific operating conditions, a comprehensive parametric study was conducted. Five key operational parameters were considered: applied voltage, temperature, gas bubble coverage, Faradaic efficiency, and the captured hydroxide ions factor. By varying these parameters, the study provides a holistic understanding of system behavior. The outputs analyzed include the evolution of hydroxide ions (OH^-) and hydrogen gas (H_2), along with the characterization of resistance components: the diaphragm resistance, anodic resistance, and cathodic resistance. This approach enables a comparative evaluation of the impact of electrode activation on the overall electrochemical performance across a range of realistic operating conditions.

Fig.6 reports the variation of the three resistance components, namely the anodic, diaphragm and cathodic resistances, over time under varying operating conditions of voltage, temperature, gas bubble coverage, Faradaic efficiency, and the captured hydroxide ions factor for activated and non-activated anodes.

Starting with the voltage effect, represented on Fig.6(a), it is noticed that the cathode resistance is the predominant component in both non-activated and activated anode scenarios, followed by the diaphragm resistance, then the anode resistance. This case is even verified when exploring the resistances variations with all the operating conditions covered by the parametric study. This trend is explained by the fact that the pores of the cathode are solely affected by the formation of free OH- and Na+ in the catholyte, while the diaphragm conductivity is influenced by both anolyte and catholyte ionic compositions, the anolyte being quasi-stable and rich of Na+ and Cl- ions. The anode, on the other hand, is permanently in contact with brine solution, offering a significant conductivity through the pores of the carbon foam material and inducing a very low anodic resistance.

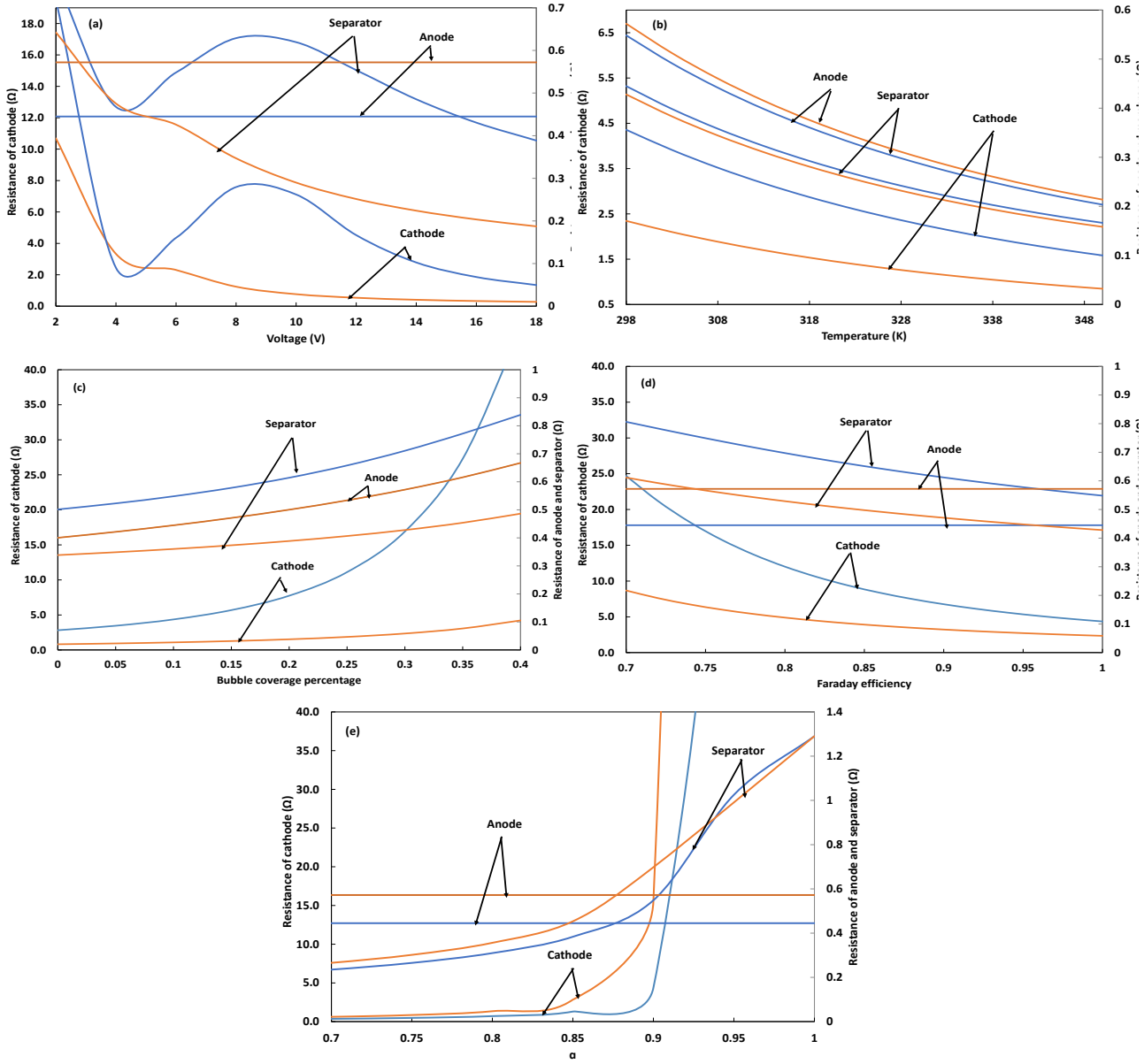

Figure 6 Parametric Analysis of anodic, diaphragm and cathodic resistance kinetics under varying operating conditions for activated and non-activated anodes

Back to the variation as a function of the operating voltage, it is well observed that the anode resistance is not affected, due to its stable conductivity components (solid porous material and anolyte filling the pores). In the contrary, the separator and cathode resistances show similar trends with non-activated anode, and also similar trends with activated anode, with the upper hand to cathode resistance as indicated previously. The separator and cathode resistances demonstrate under the non-activated anode scenario an initial decrease while rising the applied potential, then a significant increase passing by a maximum around 8 V, followed by a monotonous decrease over the studied potential range. This interesting behavior proves that the non-activated anode scenario leads to a significant increase of the ohmic resistance in the region of 4 to 9 V, explained by a chain mechanism. The non-activated anode scenario is associated with a larger activation zone as shown in the polarization curve reported earlier in Fig.1. This means a slight increase of the current while the voltage evolves within the range of 4 to 9 V. In parallel to this stagnation, the captured hydroxide ions factor increases exponentially, limiting the concentration of free hydroxide ions in the medium, which lowers the conductivity of the catholyte and consequently increases the resistance of the cathode and the diaphragm. Starting from 9 V, the current increases significantly as the voltage raises in the range if 9 to 18 V, improving the HER and the available hydroxide ions in the catholyte, which improves the conductivity and reduces the resistances of the cathode and the diaphragm.

This mechanism is suppressed when activating the anode, as the activation zone becomes thinner, and the current evolves rapidly as the applied potential increases. The balance of hydroxide ions formed by the HER reaction and captured by chemical and physical pathways is in the favor of the free ions availability in the catholyte, which results in a monotonous decrease of the cathode and diaphragm resistances as the applied potential increases.

Passing now to the effect of the cell temperature on the ohmic resistance components, it is observed from Fig.6(b) that the temperature increase induces a slight variation of the anode and diaphragm resistances, that can be negligible. The significant impact is noticed with the cathode resistance, that decreases of 46%. The effect of the temperature is attributed to two principal pathways, first, the temperature has a positive effect on the electrochemical kinetics, second, it also positively affects the nickel foam and catholyte intrinsic conductivity, which reduces the resistances [28], [29].

The third figure, i.e., Fig.6(c), demonstrates the evolution of the resistance components as a function of the bubble coverage percentage. It is noticed that while the bubble coverage increases from 0 to 40%, all the resistances increase, either under activated or non-activated anode scenarios. However, the most significant effect is associated with the cathodic resistance with non-activated anode. The increase of the resistance is expected, as the electrochemical active surface is reduced when the bubble accumulates on the electrodes, preventing good

electrochemical kinetic performance and impacting negatively the whole chain mechanism presented earlier. The activation significantly reduces the effect of the bubble accumulation on the cathodic resistance[30]. The improvement in the overall kinetics upon anode activation seems to overcome the significant reduction in the active surface [30].

The fourth figure, namely Fig.6(d), reports the evolution of the resistance components as a function of the Faradic efficiency. Though the range of current densities is not plausible for Faradic efficiency significantly lower than 1 (experiments demonstrated indeed a unit value for the Faraday efficiency for all the studied cases), the numerical study is performed to figure out the effect of this parameter if varying to low values, specifically until 0.7. Visibly, the anode resistance is not impacted by the reduction of the Faradic efficiency, which is explained by its stable conductivity components in the solid material and the anolyte filling the pores[31]. At the opposite, the diaphragm and the cathode resistances are significantly impacted, these resistances increase with the decrease of the Faradic efficiency, particularly under the non-activated anode scenario, where reducing efficiency from 1 to 0.7 leads to a dramatic 460% rise in cathode resistance. This jump is primarily due to increased side reactions such as hydrogen recombination which lower the effective ionic flux through the cathode, thereby increasing its ionic resistance[32]. Activation of the anode mitigates this effect by approximately half, likely by reducing parasitic reactions and encouraging a more uniform current distribution at the cathode surface[33]. The diaphragm resistance shows a more moderate 48 % increase over the same efficiency drop. This is attributed to a reduced ionic driving force across the membrane when fewer electrons contribute to useful gas production thus lowering electrolyte conductivity within the diaphragm's pores[34]. Anode activation further reduces this discrepancy by about 23 %, possibly by stabilizing overall cell performance and maintaining more effective ionic pathways across the membrane[34].

The last figure, Fig.6(e), shows the variation of the ohmic resistance components vs. the captured hydroxide ions factor α in the cathodic compartment, which may occur through physical and chemical mechanisms. The availability of free hydroxide ions in the cathodic compartment plays a major role in the improvement of the conductivity of the cathode, and hence, the capture of OH- by any of the plausible mechanisms interferes with the pores filling and the resistance reduction. The impact of the factor α becomes dramatic when its value reaches 0.9, making the cathodic resistance harshly increasing and the diaphragm resistance raising significantly, even with the active anode scenario.

Figs.7 and 8 present the influence of various operating parameters on OH^- and H_2 production, respectively, for both activated and non-activated anodes. A global examination confirms that the activated electrode systematically outperforms its non-activated counterpart, aligning with theoretical expectations on surface activation: enhanced electrocatalytic properties, improved

wettability, higher surface area, and reduced overpotentials. These factors collectively drive more efficient electrochemical reaction for OH^- and H_2.

At low voltages (2–5 V), both Fig.7(a) and Fig.8(a) show that activated and non-activated anodes yield similar production levels. This indicates that the system operates near the onset of electrolysis, where activation benefits are not yet fully expressed. As voltage increases, however, activated anodes exhibit exponential increases in both OH^- and H_2 generation, while the non-activated electrode responds more sluggishly, only accelerating at higher thresholds. This highlights the crucial role of applied voltage in reducing activation barriers and accelerating charge transfer reactions. The activated anode, having lower overpotential and greater surface reactivity, utilizes increased voltage more efficiently, leading to superior performance in both compartments.

Temperature exerts a positive influence on both OH^- in Fig.7(b) and H_2 in Fig.8(b) production. The activated electrode shows a much steeper increase, achieving up to 62% more output than the non-activated one at higher temperatures. This is explained by the Arrhenius relationship, where elevated temperatures enhance ion mobility, lower electrolyte viscosity, and increase reaction kinetics. The benefits are more pronounced on the activated surface, which can better exploit thermal energy due to its open structure and rich catalytic sites.

As shown in Figs.7(c) and 8(c), increasing Faradaic efficiency results in a directly proportional rise in both OH^- and H_2 production. This is because it represents the percentage of current dedicated to the target electrochemical reaction. A higher value means less current is wasted on side reactions, thus improving the overall system productivity. Across the entire range, activated anodes maintain superior output, reaffirming their role in promoting charge selectivity and conversion efficiency.

The bubble coverage factor demonstrates a strong negative impact on both OH^- and H_2 production, as shown in Figs.7(d) and 8(d). Increasing ε_{bubble} leads to more of the electrode surface being blocked by gas bubbles, which act as physical and electrical barriers between the electrode and electrolyte. This reduces the active surface area available for electrochemical reactions and increases local resistance. While the activated electrode demonstrates greater tolerance due to faster bubble detachment and improved wetting properties it also experiences efficiency loss under severe gas accumulation.

Lastly, OH- capture factor in Figs.7(e) and 8(e) has the most negative effect on both OH^- and H_2 production. As this factor increases, a sharp decline is observed in the production rates of OH^- and H_2, even though anode activation results in a 16% improvement an effect that becomes negligible at higher OH^- capture values. This decline is primarily attributed to surface adsorption, where OH^- ions are retained within the pores of the nickel electrode, thereby

limiting the available reactive surface area and displacing potential HER sites. Additionally, this phenomenon can accelerate electrode corrosion, which over time diminishes the electrode's electrochemical performance and reduces ion exchange efficiency.

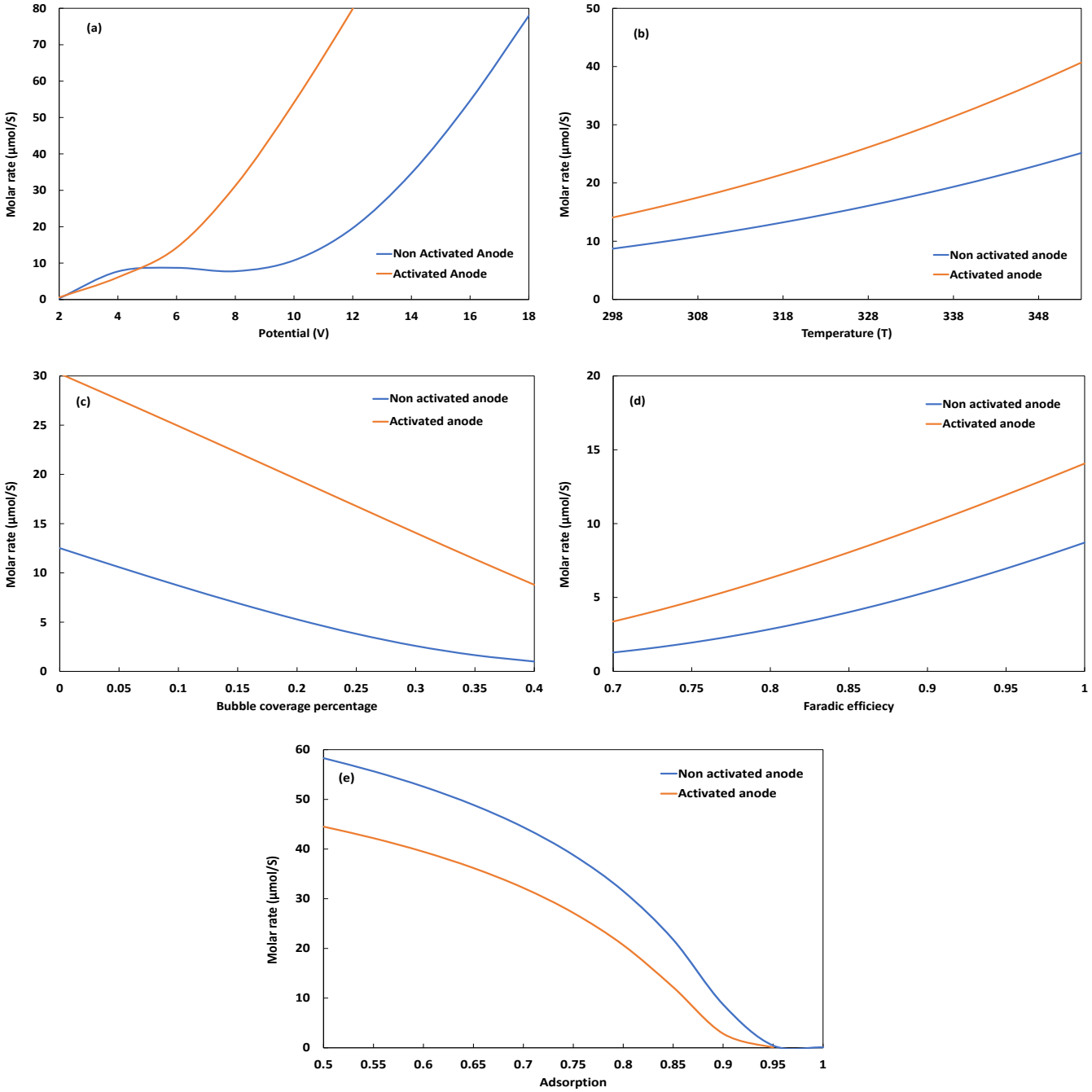

Figure 7 Parametric Analysis of Free OH^- Kinetics Under Varying Operating Conditions for Activated and Non-Activated Anodes

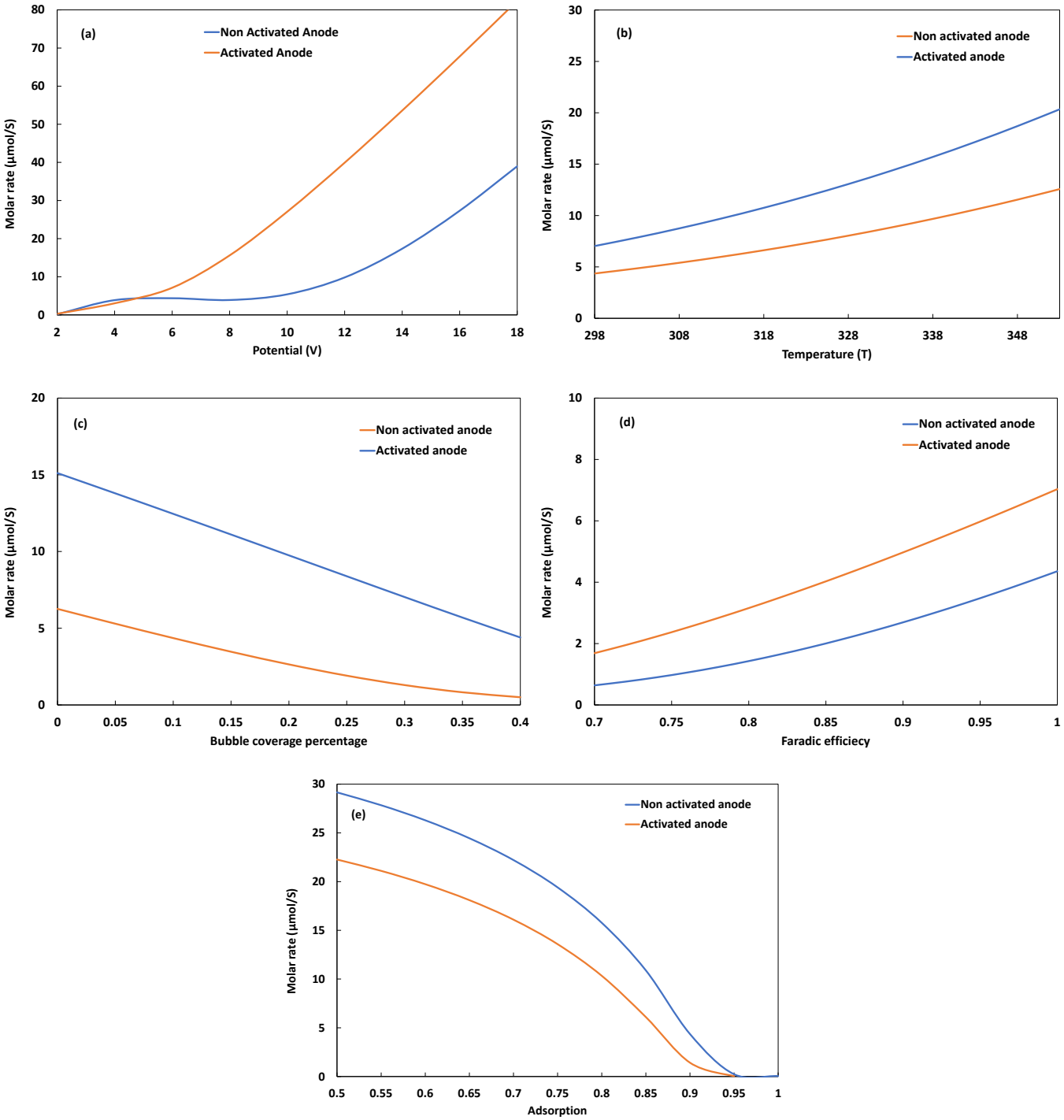

Figure 8 Parametric Analysis of H_2 Kinetics Under Varying Operating Conditions for Activated and Non-Activated Anodes

General conclusion and perspectives

This work has addressed one of the pressing challenges facing seawater desalination: the sustainable management and valorization of reverse osmosis (RO) brine. While desalination is essential to meet freshwater demands in water-scarce regions like Algeria, the process generates large quantities of hypersaline waste, which, if left untreated, poses serious environmental risks. This study proposed and investigated a promising solution: the integration of brine electrolysis using an asymmetric zero-gap electrolyzer, powered by renewable energy, to recover valuable chemical products such as hydrogen (H_2), hydroxide ions (OH^-), and hypochlorous ion (ClO-).

By combining experimental data from the UTE Desaladora plant in Skikda with a robust MATLAB-based numerical model, the project achieved a comprehensive understanding of the electrochemical and transport phenomena governing the system's behavior. The modeling phase integrated key physicochemical parameters such as temperature, applied voltage, bubble coverage, Faradaic efficiency, and OH- capture factor effects. The study provided insights into the mechanisms driving performance losses and improvements.

One of the most significant outcomes was the demonstration of the positive impact of anode activation. By modifying the anode surface with $Ni(OH)_2$, the anodic exchange current was altered, which also influenced the hydroxide capture factor. The system's internal resistance was notably reduced, enhancing both H_2 and OH^- production rates. Specifically, anode activation resulted in a 60% increase in hydrogen generation, a reduction in ohmic losses of over 55%, and improved ionic conductivity across the cathode and diaphragm. This confirmed the viability of low-cost electrode modifications as a means of boosting performance.

However, the project also highlighted the limitations of idealized simulations when compared to real-world behavior. Discrepancies (especially in current evolution and OH^- concentration) revealed the importance of integrating bubble dynamics, ion adsorption, and secondary reactions into future models. These insights emphasize that electrochemical systems designed for brine valorization must be evaluated holistically, with attention to both electrochemical and environmental performance.

References

[1] L. El Amine, “Seawater Desalination in Algeria: A Comprehensive Assessment of its Viability as a Water Security Strategy,” *Revue Le Manager*, vol. 10, p. 2023, 2023.

[2] H. Shemer, S. Wald, and R. Semiat, “Challenges and Solutions for Global Water Scarcity,” Jun. 01, 2023, *MDPI*. doi: 10.3390/membranes13060612.

[3] K. E. Ojaomo, T. J. Erinle, D. H. Oladebeye, and O. D. Olakolegan, “Hydrogen Generation through Electrolysis of Brine for Clean Energy Development in a Depressed Economy,” *IARJSET*, vol. 7, no. 4, pp. 94–101, Apr. 2020, doi: 10.17148/iarjset.2020.7415.

[4] A. Kumar, K. R. Phillips, J. Cai, U. Schröder, and J. H. Lienhard, “Integrated Valorization of Desalination Brine through NaOH Recovery: Opportunities and Challenges,” *Angewandte Chemie*, vol. 131, no. 20, pp. 6570–6579, May 2019, doi: 10.1002/ange.201810469.

[5] R. Phillips and C. Dunnill, “Zero Gap Cell Design for Alkaline Electrolysis”, doi: 10.13140/RG.2.2.26663.29606.

[6] M. T. de Groot and A. W. Vreman, “Ohmic resistance in zero gap alkaline electrolysis with a Zirfon diaphragm,” *Electrochim Acta*, vol. 369, Feb. 2021, doi: 10.1016/j.electacta.2020.137684.

[7] J. W. Haverkort and H. Rajaei, “Voltage losses in zero-gap alkaline water electrolysis,” *J Power Sources*, vol. 497, Jun. 2021, doi: 10.1016/j.jpowsour.2021.229864.

[8] R. Belhadj Ammar *et al.*, “A New Method Based on a Zero Gap Electrolysis Cell for Producing Bleach: Concept Validation,” *Membranes (Basel)*, vol. 12, no. 6, Jun. 2022, doi: 10.3390/membranes12060602.

[9] C. Henao, K. Agbossou, M. Hammoudi, Y. Dubé, and A. Cardenas, “Simulation tool based on a physics model and an electrical analogy for an alkaline electrolyser,” 2014, *Elsevier B.V.* doi: 10.1016/j.jpowsour.2013.10.086.

[10] P. Colbertaldo, S. L. Gómez Aláez, and S. Campanari, “Zero-dimensional dynamic modeling of PEM electrolyzers,” in *Energy Procedia*, Elsevier Ltd, 2017, pp. 1468–1473. doi: 10.1016/j.egypro.2017.12.594.

[11] E. A. Shulaeva, N. S. Shulaev, and J. F. Kovalenko, “Modeling of the process of electrolysis production of caustic, chlorine and hydrogen,” in *Journal of Physics: Conference Series*, Institute of Physics Publishing, 2017. doi: 10.1088/1742-6596/803/1/012148.

[12] Y. Tang and B. Vreman, “4WC13-BEP Power and Flow Design of a lab-scale ‘zero-gap’ water electrolyser,” 2022.

[13] Z. Zhang *et al.*, “Metallic porous electrodes enable efficient electrolysis of liquid CO 2 capture solutions.”

[14] K. E. Ojaomo, T. J. Erinle, D. H. Oladebeye, and O. D. Olakolegan, “Hydrogen Generation through Electrolysis of Brine for Clean Energy Development in a Depressed Economy,” *IARJSET*, vol. 7, no. 4, pp. 94–101, Apr. 2020, doi: 10.17148/iarjset.2020.7415.

[15] A. Vedrtnam, K. Kalauni, and R. Pahwa, “Water Electrolysis Technologies and Their Modeling Approaches: A Comprehensive Review,” Apr. 01, 2025, *Multidisciplinary Digital Publishing Institute (MDPI)*. doi: 10.3390/eng6040081.

[16] “Fabricants, fournisseurs, usine de mousse de nickel en Chine - Hebei Boni.”

[17] “Temperature Coefficient of Resistance | Physics Of Conductors And Insulators | Electronics Textbook.”

[18] M. Blal, A. Benatillah, A. Belasri, A. Bouraiou, S. Lachtar, and R. Dabou, “Study of hydrogen production by solar energy as tool of storing and utilization renewable energy for the desert areas,” *Int J Hydrogen Energy*, vol. 41, no. 45, pp. 20788–20806, 2016, doi: 10.1016/j.ijhydene.2016.07.034.

[19] R. L. Leroy, C. T. Bowen, P. Claire, C. H. Ig, and D. J. Leroy, “The thermodynamics of aqueous water electrolysis,” *J. Electrochem. Soc.*, vol. 127, no. 9, pp. 1954–1962, 1980.

[20] C. Henao, K. Agbossou, M. Hammoudi, Y. Dubé, and A. Cardenas, “Simulation tool based on a physics model and an electrical analogy for an alkaline electrolyser,” *J Power Sources*, vol. 250, pp. 58–67, 2014, doi: 10.1016/j.jpowsour.2013.10.086.
[21] M. Hammoudi, C. Henao, K. Agbossou, Y. Dubé, and M. L. Doumbia, “New multi-physics approach for modelling and design of alkaline electrolyzers,” *Int J Hydrogen Energy*, vol. 37, no. 19, pp. 13895–13913, 2012, doi: 10.1016/j.ijhydene.2012.07.015.
[22] W. Wang, X. Wei, D. Choi, X. Lu, G. Yang, and C. Sun, “Chapter 1 - Electrochemical cells for medium- and large-scale energy storage: fundamentals,” in *Woodhead Publishing Series in Energy*, C. Menictas, M. Skyllas-Kazacos, and T. M. B. T.-A. in B. for M. and L.-S. E. S. Lim, Eds., Woodhead Publishing, 2015, pp. 3–28. doi: https://doi.org/10.1016/B978-1-78242-013-2.00001-7.
[23] Y. Tang, T. Zhang, X. Wu, and S. Deng, “Active Sites Regulation for High-Performance Oxygen Evolution Reaction Electrocatalysts,” Apr. 27, 2022, *Frontiers Media S.A.* doi: 10.3389/fchem.2022.889470.
[24] H. H. I. Eltigani and Y. Boonyongmaneerat, “Progress of water desalination applications based on wettability and surface characteristics of graphene and graphene oxide: A review,” *Journal of Metals, Materials and Minerals*, vol. 32, no. 3, pp. 15–26, 2022, doi: 10.55713/jmmm.v32i3.1520.
[25] Q. Pan, P. Zhao, L. Gao, H. Liu, H. Hu, and L. Dong, “In-Depth Study on the Effects of Impurity Ions in Saline Wastewater Electrolysis,” *Molecules*, vol. 28, no. 12, Jun. 2023, doi: 10.3390/molecules28124576.
[26] A. M. Oliveira, B. P. Setzler, and Y. Yan, “Study of pH Gradients and Carbonation of Hydroxide Exchange Membrane Electrolyzers,” *J Electrochem Soc*, vol. 172, no. 2, p. 024509, Feb. 2025, doi: 10.1149/1945-7111/adb51d.
[27] R. Subbaraman *et al.*, “Enhancing hydrogen evolution activity in water splitting by tailoring Li+-Ni(OH)2-Pt interfaces,” *Science (1979)*, vol. 334, no. 6060, pp. 1256–1260, Dec. 2011, doi: 10.1126/science.1211934.
[28] M. H. Miles, G. Kissel, P. W. T. Lu, and S. Srinivasan, “Effect of Temperature on Electrode Kinetic Parameters for Hydrogen and Oxygen Evolution Reactions on Nickel Electrodes in Alkaline Solutions,” *J Electrochem Soc*, vol. 123, no. 3, pp. 332–336, Mar. 1976, doi: 10.1149/1.2132820.
[29] A. Barroso-Bogeat, M. Alexandre-Franco, C. Fernández-González, A. Macías-García, and V. Gómez-Serrano, “Temperature dependence of the electrical conductivity of activated carbons prepared from vine shoots by physical and chemical activation methods,” *Microporous and Mesoporous Materials*, vol. 209, pp. 90–98, Jun. 2015, doi: 10.1016/j.micromeso.2014.07.023.
[30] A. Angulo, P. van der Linde, H. Gardeniers, M. Modestino, and D. Fernández Rivas, “Influence of Bubbles on the Energy Conversion Efficiency of Electrochemical Reactors,” Mar. 18, 2020, *Cell Press*. doi: 10.1016/j.joule.2020.01.005.
[31] M. E. Kreider *et al.*, “Understanding the Effects of Anode Catalyst Conductivity and Loading on Catalyst Layer Utilization and Performance for Anion Exchange Membrane Water Electrolysis,” *ACS Catalysis* , vol. 14, no. 14, pp. 10806–10819, Jul. 2024, doi: 10.1021/acscatal.4c02932.
[32] W. Li, H. Tian, L. Ma, Y. Wang, X. Liu, and X. Gao, “Low-temperature water electrolysis: fundamentals, progress, and new strategies,” May 17, 2022, *Royal Society of Chemistry*. doi: 10.1039/d2ma00185c.
[33] P. S. Gaikwad, K. Mondal, Y. K. Shin, A. C. T. van Duin, and G. Pawar, “Enhancing the Faradaic efficiency of solid oxide electrolysis cells: progress and perspective,” Dec. 01, 2023, *Nature Research*. doi: 10.1038/s41524-023-01044-1.
[34] B. Yodwong, D. Guilbert, M. Phattanasak, W. Kaewmanee, M. Hinaje, and G. Vitale, “Faraday’s efficiency modeling of a proton exchange membrane electrolyzer based on experimental data,” *Energies (Basel)*, vol. 13, no. 18, Sep. 2020, doi: 10.3390/en13184792.

Appendix

Table 2 Adopted parameters in the numerical procedure

Study	**Parameter**		**value**	**Output**
Polarization curve	Voltage		2,4,6,8,10,12,14,16,18 V	I_{max}
	Temperature		25°C	
	ε_{bubble}		0%	
	Faradic efficiency		100%	
	α	Non-activated	0.48, 0.75, 0.87, 0.92, 0.94, 0.95, 0.96, 0.96, 0.96	
		Activated	0.26, 0.75, 0.84, 0.86, 0.86, 0.86, 0.86, 0.86, 0.86	
Performance benchmark	Voltage		6 V	ε_{bubble} for I match to experimental
	Temperature		25°C	
	Faradic efficiency		100%	
	α	Non-Activated	0.87	
		Activated	0.84	
Parametric study	Voltage		2, 4, 6, 8, 10, 12, 14, 16, 18 V	$R_{mem}, R_a, R_c, R_{ohm}$, $\dot{n}_{H_2}, \dot{n}_{HO^-}, I_{max}$
	Temperature		25, 30, 35, 40, 45, 50, 55, 60, 65, 70, 75, 80°C	
	ε_{bubble}		0, 0.05, 0.1, 0.15, 0.2, 0.25, 0.3, 0.35, 0.4	
	Faradic efficiency		70, 72, 74, 76, 78, 80, 82, 84, 86, 88, 90, 92, 94, 96, 98, 100%	
	α		0.5, 0.55, 0.6, 0.65, 0.7, 0.75, 0.8, 0.85, 0.9, 0.95, 1	
	Time		0, 5, 10, 15, 20, 25, 30min	